

Modeling of Depth of Interaction with Inter-crystal Scattering for PET Reconstruction

László Szirmay-Kalos, Dóra Varnyú, Milán Magdics, and Balázs Tóth

Abstract—Depth of Interaction (DOI) PET scanners extend the data stored about photon detection events by the depth of the gamma photon’s absorption in the detector crystals. Popular DOI-based reconstruction methods disregard photon scattering in the detectors and simply modify the endpoints of the Lines of Responses (LORs). However, such simplification reduces the accuracy of the resulting image. This paper proposes the incorporation of the modeling of inter-crystal scattering into DOI-based PET reconstructions. The transfer probabilities caused by inter-crystal scattering are determined off-line with Monte Carlo simulation and are built into the system matrix as a factored component.

I. INTRODUCTION

During a Positron Emission Tomography (PET) scan, the task is to determine the spatial distribution of the radiotracer in the observed object. The input of the computations is the number of simultaneous gamma photon hits in detector crystal pairs, also called Lines of Responses (LORs). In iterative ML-EM reconstruction, the expected numbers of coincidences are computed by simulating the particle transport, and the estimation of the tracer distribution is corrected according to the ratio of computed and measured coincidence numbers [1], [2]. This process is then repeated until convergence. Depth of Interaction (DOI) measurements provide additional information about the depth of the gamma photon’s absorption in the detector crystal, which can be exploited to reduce parallax errors caused by handling detector crystals as single points [3], [4], [5]. However, DOI-based reconstruction approaches disregard the fact that photons can scatter inside the detectors.

We propose a *factored method* to incorporate DOI information into the system matrix, which is able to deal with inter-crystal scattering. We also address the challenge of efficient processing of the increased number of LORs by applying randomization.

II. PREVIOUS WORK

The input of PET reconstruction is the list of coincidence events defined by pairs of detector crystals. If we can identify

Manuscript received December 20, 2020. This work has been supported by OTKA K-124124, Vekop-221-16, and by the EFOP-3.6.1-16-2016-00014 project financed by the Ministry of Human Capacities.

L. Szirmay-Kalos is with the Budapest University of Technology and Economics, Hungary (e-mail: szirmay@iit.bme.hu)

D. Varnyú is with the Budapest University of Technology and Economics, Hungary (e-mail: varnyu.dora@iit.bme.hu)

M. Magdics is with the Budapest University of Technology and Economics, Hungary (e-mail: magdics@iit.bme.hu)

B. Tóth is with the Budapest University of Technology and Economics, Hungary (e-mail: tbalazs@iit.bme.hu)

not only the detector crystals of gamma photon absorption, but also the depth of the absorption, then parallax errors caused by the incorrect identification of the endpoints of the LOR can be greatly reduced [6]. During recent years, many different estimation techniques have been developed to obtain this information [7], [8], [9], [10], [11], [5], [12].

Depth of Interaction information can be regarded as partitioning the detector crystals into N_D depth layers, which increases the number of LORs by a factor of N_D^2 [13]. The LORs introduced this way intersect the field of view non-uniformly, and significantly increase the density far from the center, thus this is where DOI produces the highest improvement. However, the non-uniformity of LORs pose problems in filtered back projection, which needs sinogram re-binning [14]. In ML-EM based approaches, the significantly larger system matrix results in higher reconstruction time, and irregular sampling in noise. Thus re-binning aims at the reduction of both noise and computation time [15], [13].

During reconstruction, the photon transport inside the detector crystals needs to be considered, where so far only attenuation effects have been modeled [16], [17], [18]. In this paper, we extend this model with the Rayleigh and Compton scattering effect, and propose an efficient computation scheme for it.

III. FACTORED METHOD

In a single iteration cycle of an ML-EM reconstruction, a forward projection and a back projection are executed. The *forward projection* computes the expected number of coincidences \tilde{y}_L in LOR L assuming the currently estimated activities x_V of voxel V :

$$\tilde{y}_L = \sum_V \mathbf{A}_{L,V} x_V$$

where $\mathbf{A}_{L,V}$ is the element of the *system matrix* representing the probability that a decay in voxel V causes a coincidence in LOR L .

Back projection corrects the voxel estimates from x_V to x'_V according to the following formula that increases the likelihood assuming Poisson distributed coincidences:

$$x'_V = x_V \frac{\sum_L \mathbf{A}_{L,V} \frac{y_L}{\tilde{y}_L}}{\sum_L \mathbf{A}_{L,V}}$$

The system matrix establishes a correspondence between voxels and LORs, i.e. sources and detectors. As both have 3D domain, and scattering can happen anywhere in the 3D space, the contribution of sources to detectors is a high-dimensional

integral in the domain of source points, detector points and arbitrary number of scattering points. Such high-dimensional integrals are calculated by tracing sample paths. With more paths, higher precision results can be obtained.

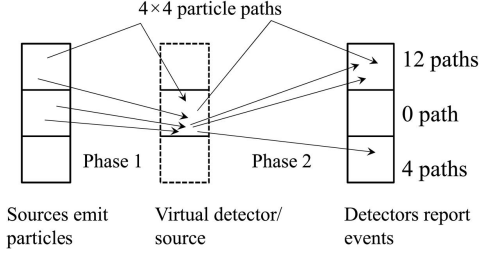


Fig. 1: Conceptual model of factoring. The particle transport process is decomposed into phases by introducing virtual virtual detectors. The simulation of all particles is first executed up to the virtual detectors, then virtual detectors become virtual sources and the second phase simulates transport from them to the real detectors.

The idea of *factoring* comes from the decomposition of the system matrix as the product of simpler matrices [19]. Factoring can also be regarded as the decomposition of the photon transport process into phases with the introduction of virtual detectors (Fig. 1) [2]. First, the expected values in the first layer of virtual detectors are computed from the source. Then, the detectors of the first layer become sources and a similar algorithm is executed until we arrive at the real detectors. The advantages of this approach are the following:

- The calculation of a single phase can be much simpler than that of the complete transport process, thus we can eliminate all conditional statements that would degrade GPU efficiency.
- As a computed sample path ending in a virtual detector is continued by all paths starting from here in the next phase, we have a much higher number of sample paths to estimate the high dimensional integral, thus the result is more accurate (in Fig. 1 the number of paths has increased from 4 to 16).
- Each phase is computed in parallel on the GPU, where threads do not communicate with each other. However, the next phase can reuse the results of all the threads of the previous phase, so redundant computations can be eliminated.

The disadvantage of factoring is that virtual detectors discretize the continuous space, so discretization error may occur.

In our proposed system, the transport process is decomposed into two factored steps:

- 1) *Geometric phase* that follows the photon pair from the annihilation point to the surfaces of two detector crystals $\mathbf{i}_1, \mathbf{i}_2$ and computes the expected number of hits $\tilde{y}_G^{\text{geom}}$ on the surfaces of the crystal surface pairs. The probability of the path from voxel V to *geometric LOR* $G = (\mathbf{i}_1, \mathbf{i}_2)$ is expressed by the geometric system matrix $\mathbf{A}_{G,V}^{\text{geom}}$, which can be estimated by standard techniques [20], [21].

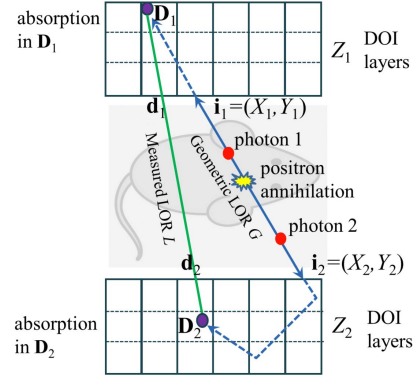


Fig. 2: Factored simulation. The photons born at the point of annihilation enter the detector at crystal surfaces indexed with \mathbf{i}_1 and \mathbf{i}_2 , then are later absorbed and detected in the pair of detector subvolumes \mathbf{D}_1 and \mathbf{D}_2 , respectively.

- 2) *Detector response* that includes all phenomena happening in the detector, including inter-crystal scattering, absorption, and the sensitivity of crystals and electronics. Here, the two absorption points form a *measured LOR* L , for which the expected number of hits \tilde{y}_L needs to be calculated. The detector phase is further decomposed into two phases. We separately consider the gamma photon transport until absorption and the phenomena after gamma photon absorption until the output of the electronics separating coincidence events. The first phase depends on the direction of the LOR, the second phase on the crystal and on the module pair of the two crystals. The probability of absorption in measured LOR L of a photon pair arriving at the respective detector surfaces of geometric LOR G is denoted by *LOR transfer probability* $p_{G \rightarrow L}$. On the other hand, crystal sensitivities and the dead-time parameter are lumped into a single *sensitivity* ε_L associated with measured LOR L , which expresses the expected number of reported events when an absorption happens at the two ends of this LOR.

These steps are combined together in the system matrix

$$\mathbf{A}_{L,V} = \varepsilon_L \sum_G p_{G \rightarrow L} \mathbf{A}_{G,V}^{\text{geom}}. \quad (1)$$

Note that during the geometric phase, we need to compute only the geometric LORs, which are significantly fewer than the real LORs, which reduces the computation time.

A. Calculation of the LOR transfer probabilities

Detector crystals are on planar modules and their visible surfaces form a 2D grid. A single detector crystal surface can be identified by a pair of integer coordinates $\mathbf{i} = (X, Y)$. Each crystal is further decomposed by the depth layers into crystal subvolumes. The composition of the surface index and the depth layer uniquely identify the subvolume, which altogether requires three integer coordinates: $\mathbf{D} = (\mathbf{d}, Z) = (X, Y, Z)$, where Z is the depth layer index.

The fact that a photon enters a crystal does not necessarily mean that the photon is absorbed in this crystal. This phenomenon can be modeled by *detector transport probability* $p_{\mathbf{i} \rightarrow \mathbf{D}}(\theta, \phi)$, which specifies the conditional probability that a photon is absorbed in crystal subvolume \mathbf{D} provided that it arrived at crystal surface \mathbf{i} from the direction given by angles θ and ϕ with the normal and axial directions of the detector module, respectively (Fig. 2).

We assume that crystals are similar, thus this probability depends just on the translation $\mathbf{t} = \mathbf{d} - \mathbf{i}$ between crystal surfaces and on depth layer Z of absorption:

$$p_{\mathbf{i} \rightarrow (\mathbf{d}, Z)}(\theta, \phi) = \Pr\{\mathbf{d} - \mathbf{i}, Z | \theta, \phi\} = \Pr\{\mathbf{t}, Z | \theta, \phi\}.$$

Suppose that the visible surfaces of detector crystals are small with respect to the distance of the detector modules, so direction (θ, ϕ) of the LOR is constant for those crystals which are in the neighborhood of \mathbf{d} and where $p_{\mathbf{i} \rightarrow \mathbf{D}}$ is not negligible.

The sum of the detector transport probabilities of a DOI layer is the *layer detection probability*, i.e. the probability that the photon gets absorbed in this layer:

$$\nu(Z, \theta, \phi) = \Pr\{Z | \theta, \phi\} = \sum_{\mathbf{t}} \Pr\{\mathbf{t}, Z | \theta, \phi\}. \quad (2)$$

Combining the detector transport probabilities at the two ends of the LOR, we obtain the LOR transport probability from geometric LOR $G = (\mathbf{i}_1, \mathbf{i}_2)$ to measured LOR $L = (\mathbf{D}_1, \mathbf{D}_2)$:

$$p_{G \rightarrow L} = p_{\mathbf{i}_1 \rightarrow \mathbf{D}_1}(\theta_1, \phi_1) p_{\mathbf{i}_2 \rightarrow \mathbf{D}_2}(\theta_2, \phi_2). \quad (3)$$

Note that the angles θ_1, ϕ_1 and θ_2, ϕ_2 depend on the orientation of the detector modules and also on the crystal surfaces \mathbf{i}_1 and \mathbf{i}_2 where the photons enter. If the photons cannot scatter far in the crystal, we can assume that the directions are similar to the direction between absorber crystal volumes \mathbf{D}_1 and \mathbf{D}_2 .

B. LOR-centric forward projection

The expected number of hits \tilde{y}_L in measured LOR L is

$$\tilde{y}_L = \sum_V \mathbf{A}_{L,V} x_V = \varepsilon_L \sum_G p_{G \rightarrow L} \sum_V \mathbf{A}_{G,V}^{\text{geom}} x_V. \quad (4)$$

It means that in the first phase, a geometric projection is executed computing

$$\tilde{y}_G^{\text{geom}} = \sum_V \mathbf{A}_{G,V}^{\text{geom}} x_V. \quad (5)$$

Then the obtained geometric LOR values are filtered to compute the expected coincidences in measured LOR L :

$$\tilde{y}_L = \varepsilon_L \sum_G \tilde{y}_G^{\text{geom}} p_{G \rightarrow L}. \quad (6)$$

A measured LOR L is identified by the crystal indices $(\mathbf{d}_1, \mathbf{d}_2)$ and depth layer indexes (Z_1, Z_2) at the two endpoints. When \tilde{y}_L is computed, $(\mathbf{d}_1, \mathbf{d}_2)$ and (Z_1, Z_2) are known and fixed, so are the directions defined by θ_1, ϕ_1 and θ_2, ϕ_2 if we use the assumption that the LOR is much longer than the mean free path of gamma photons in the detector crystals. For these fixed parameters, we should sum a large number of potential geometric LORs G , i.e. $(\mathbf{i}_1, \mathbf{i}_2)$ pairs.

The filtering is evaluated by Monte Carlo estimation taking M random samples of crystal surface offsets $(\mathbf{t}_1(1), \mathbf{t}_2(1)), (\mathbf{t}_1(2), \mathbf{t}_2(2)), \dots, (\mathbf{t}_1(M), \mathbf{t}_2(M))$ between the crystal indices of observed and geometric LORs:

$$\tilde{y}_L \approx \frac{\varepsilon_L}{M} \sum_{s=1}^M \frac{\tilde{y}_{G(s) \rightarrow L}^{\text{geom}} p_{G(s) \rightarrow L}}{\Pr\{G(s) | L\}} \quad (7)$$

where $G(s) = (\mathbf{d}_1 - \mathbf{t}_1(s), \mathbf{d}_2 - \mathbf{t}_2(s))$, and $\Pr\{G(s) | L\} = \Pr\{\mathbf{t}_1(s), \mathbf{t}_2(s) | L\}$ is the probability of sample s . A sample is associated with a pair of offset vectors $\mathbf{t}_1 = \mathbf{d}_1 - \mathbf{i}_1$ and $\mathbf{t}_2 = \mathbf{d}_2 - \mathbf{i}_2$ and its selection probability can also depend on the DOI depths Z_1 and Z_2 . We sample offset vectors \mathbf{t}_1 and \mathbf{t}_2 with probabilities $\Pr\{\mathbf{t}_1 | Z_1, \theta_1, \phi_1\}$ and $\Pr\{\mathbf{t}_2 | Z_2, \theta_2, \phi_2\}$, independently:

$$\Pr\{\mathbf{t}_1, \mathbf{t}_2 | L\} = \Pr\{\mathbf{t}_1 | Z_1, \theta_1, \phi_1\} \Pr\{\mathbf{t}_2 | Z_2, \theta_2, \phi_2\}.$$

Sample generation is discussed in Section IV.

Such sampling is an *importance sampling* [21], since sample probabilities are proportional to $p_{G(s) \rightarrow L}$. To prove this, let us consider one of the two endpoints of the LOR:

$$\Pr\{\mathbf{t} | Z, \theta, \phi\} = \frac{\Pr\{\mathbf{t}, Z | \theta, \phi\}}{\Pr\{Z | \theta, \phi\}} = \frac{p_{\mathbf{i} \rightarrow \mathbf{D}}}{\nu(Z, \theta, \phi)}.$$

Substituting this probability into Eq. 7 and using Eq. 3, the final estimator of the expected coincidences is

$$\tilde{y}_L \approx \varepsilon_L \frac{\nu(Z_1, \theta_1, \phi_1) \nu(Z_2, \theta_2, \phi_2)}{M} \sum_{s=1}^M \tilde{y}_{G(s)}^{\text{geom}}. \quad (8)$$

It means that after the geometric first pass, the 4D LOR map is filtered separately for every combination of depth layers Z_1, Z_2 . Each computation thread takes one measurable LOR L and calculates \tilde{y}_L by adding the sampled geometric LORs.

C. Voxel-centric back projection

In the back projection of ML-EM reconstruction, we have to evaluate the numerator $\sum_L \mathbf{A}_{L,V} \frac{y_L}{\tilde{y}_L}$ and the denominator $\sum_L \mathbf{A}_{L,V}$ of the scaling factor for each voxel.

Let us consider the numerator and substitute the factorization of the system matrix into its expression:

$$\begin{aligned} \sum_L \mathbf{A}_{L,V} \frac{y_L}{\tilde{y}_L} &= \sum_G \mathbf{A}_{G,V}^{\text{geom}} \sum_L p_{G \rightarrow L} \varepsilon_L \frac{y_L}{\tilde{y}_L} \\ &= \sum_G \mathbf{A}_{G,V}^{\text{geom}} r_G. \end{aligned} \quad (9)$$

It means that instead of back projecting the ratios of measured LORs y_L / \tilde{y}_L , first these ratios participate in a filtering like operation, which constitutes the first phase of the numerator calculation:

$$\begin{aligned} r_G &= \sum_L p_{G \rightarrow L} \varepsilon_L \frac{y_L}{\tilde{y}_L} = \sum_{Z_1, Z_2} \sum_{\mathbf{d}_1, \mathbf{d}_2} p_{G \rightarrow L} \varepsilon_L \frac{y_L}{\tilde{y}_L} \\ &= \sum_{Z_1, Z_2} r_G(Z_1, Z_2) \end{aligned}$$

where LOR L is defined by detector subvolumes (\mathbf{d}_1, Z_1) and (\mathbf{d}_2, Z_2) .

For the depth layers Z_1 and Z_2 we use a full summation. However, the sum of detector crystals $\mathbf{d}_1, \mathbf{d}_2$ is evaluated by Monte Carlo method. Now we have $G = (\mathbf{i}_1, \mathbf{i}_2)$ and the depth indices (Z_1, Z_2) fixed and should sample measured LOR L , i.e. generate random offsets \mathbf{t}_1 and \mathbf{t}_2 and obtain detector indices as $\mathbf{d}_1 = \mathbf{i}_1 + \mathbf{t}_1$ and $\mathbf{d}_2 = \mathbf{i}_2 + \mathbf{t}_2$. The estimator of the sum of detector crystals is

$$\begin{aligned} r_G(Z_1, Z_2) &= \sum_{\mathbf{d}_1, \mathbf{d}_2} p_{G \rightarrow L} \varepsilon_L \frac{y_L}{\tilde{y}_L} \\ &\approx \frac{1}{M} \sum_{s=1}^M \frac{p_{G \rightarrow L(s)} \varepsilon_{L(s)} \frac{y_{L(s)}}{\tilde{y}_{L(s)}}}{\Pr\{L(s)|G, Z_1, Z_2\}} \end{aligned} \quad (10)$$

where the probability of a sample is

$$\begin{aligned} \Pr\{L|G, Z_1, Z_2\} &= \Pr\{\mathbf{t}_1, \mathbf{t}_2|G, Z_1, Z_2\} \\ &= \Pr\{\mathbf{t}_1|Z_1, \theta_1, \phi_1\} \Pr\{\mathbf{t}_2|Z_2, \theta_2, \phi_2\} \\ &= \frac{p_{\mathbf{i}_1 \rightarrow (\mathbf{d}_1, Z_1)} p_{\mathbf{i}_2 \rightarrow (\mathbf{d}_2, Z_2)}}{\nu(Z_1, \theta_1, \phi_1) \nu(Z_2, \theta_2, \phi_2)} \\ &= \frac{p_{G \rightarrow L}}{\nu(Z_1, \theta_1, \phi_1) \nu(Z_2, \theta_2, \phi_2)}. \end{aligned} \quad (11)$$

Substituting this into Eq. 10, the first phase of the calculation of the numerator is

$$r_G(Z_1, Z_2) \approx \frac{\nu(Z_1, \theta_1, \phi_1) \nu(Z_2, \theta_2, \phi_2)}{M} \sum_{s=1}^M \varepsilon_{L(s)} \frac{y_{L(s)}}{\tilde{y}_{L(s)}}.$$

Using the results of the first phase, the estimator of the numerator of the back projection formula is:

$$\sum_L \mathbf{A}_{L,V} \frac{y_L}{\tilde{y}_L} \approx \sum_L \mathbf{A}_{G,V}^{\text{geom}} \sum_{Z_1, Z_2} r_G(Z_1, Z_2).$$

The denominator can be calculated by a simultaneous LOR filtering when ratios y_L/\tilde{y}_L are replaced by 1 in the first phase:

$$\begin{aligned} n_G(Z_1, Z_2) &= \sum_{\mathbf{d}_1, \mathbf{d}_2} p_{G \rightarrow L} \varepsilon_L \\ &\approx \frac{\nu(Z_1, \theta_1, \phi_1) \nu(Z_2, \theta_2, \phi_2)}{M} \sum_{s=1}^M \varepsilon_{L(s)}. \end{aligned}$$

Then, the denominator is obtained as

$$\sum_L \mathbf{A}_{L,V} \approx \sum_L \mathbf{A}_{G,V}^{\text{geom}} \sum_{Z_1, Z_2} n_G(Z_1, Z_2).$$

IV. TRANSPORT PROBABILITIES

For the 400-511 keV range gamma photons, three types of interaction with LYSO crystal material are important: photoelectric absorption, Compton, i.e. incoherent scattering and Rayleigh or coherent scattering. The cross sections at 511 keV for the photoelectric effect is $\sigma_a = 37.4^{-1} [\text{mm}^{-1}]$, for Compton scattering $\sigma_{is} = 19.1^{-1} [\text{mm}^{-1}]$ and for Rayleigh scattering $\sigma_{cs} = 214^{-1} [\text{mm}^{-1}]$. The photoelectric absorption cross section is inversely proportional to the 2.5th power of the photon energy, while the Rayleigh cross section is inversely proportional to the 1.9th power of the photon energy, thus the chances of such interaction are almost doubled as the photon loses its energy from 511 keV to 400 keV during Compton scattering. The cross section of Compton scattering

TABLE I: Detection probabilities $\sum_Z \nu(Z, \theta, \phi = 45^\circ)$ modeling photoelectric absorption and also scattering.

θ	0	15°	30°	45°	60°
Absorption	0.274	0.284	0.310	0.364	0.473
+ scattering	0.289	0.298	0.329	0.396	0.512

also increases for smaller energies as specified by the Klein-Nishina formula but its increase is less than 10% while the energy is reduced from 511 keV to 400 keV.

For 511 keV photons born at a positron-electron annihilation, Compton scattering is about two times more likely than photoelectric absorption and is about ten times more likely than Rayleigh scattering. However, at this energy range, when the energy decrease is small according to the Compton law, Compton scattering has a strong forward scattering character, thus Compton scattering changes neither the energy nor the direction most of the time. It means that its effect does not modify the properties of the gamma photons, i.e. it behaves as if it did not occur. In contrast, Rayleigh scattering modifies the direction on a larger scale and gets more relevant on lower energies. Eventually, Rayleigh scattering is responsible for dispersing the photons in a larger detector area. To quantify the difference, we compared the transport probabilities computed only with photoelectric absorption and also with Compton and Rayleigh scattering, and presented the total detection probabilities for the two models. Table I shows the detection probabilities, i.e. the sum of the transport probabilities of all crystals. During this simulation, we assumed a 400–600 keV window, i.e. photons are ignored when their energy drops below 400 keV.

Sampling according to these transport maps is supported by pre-computed tables. First, the layer detection probability maps are calculated by simulating photons arriving from a direction of given inclination and azimuth angles at uniformly distributed points on the detector surface. Having the probabilities, we pre-generate relaxed Monte Carlo offset vector sets that contain just a few samples, but their distribution is as close to the simulated distribution as possible [22], [23].

V. RESULTS

The proposed DOI reconstruction algorithm has been implemented in CUDA. We have modeled the PET system of the *NanoPET/CT 122* scanner [24], [25], which has a detector ring consisting of 12 modules. During our measurements, we used 1:3 coincidence mode, i.e. each detector module formed LORs with three opposite modules of the ring, thus there were $12 \times 3/2 = 18$ module pairs. A module contains $81 \times 39, 1.12 \times 1.12 \times 13$ mm LYSO detector crystals, which are divided into two depth layers. Therefore, the number of LORs in the entire system is $18 \times (81 \times 39 \times 2)^2 = 718$ millions.

The proposed LOR filtering method has been compared to DOI free reconstruction and to a classical DOI approach called *detector inflation* that shifts the endpoints of the LOR into the crystals. The *cross-correlation (CC)* error curves are displayed by Figs. 3–5, while Figs. 6–8 show the outputs of the reconstructions.

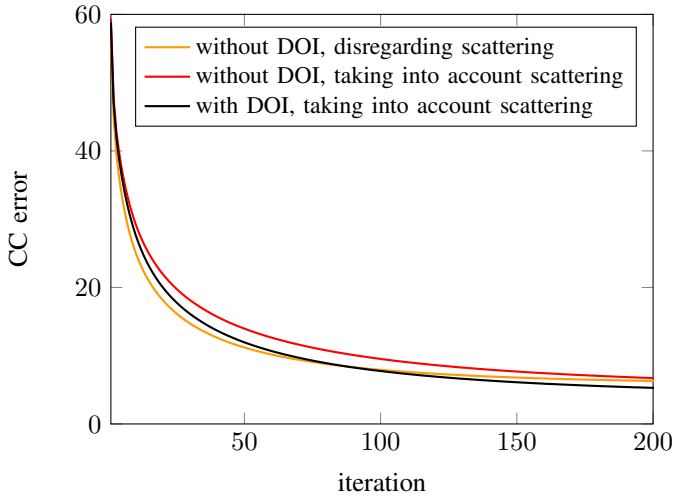


Fig. 3: CC error curves of the reconstructions, applying LOR filtering in both forward and back projections.

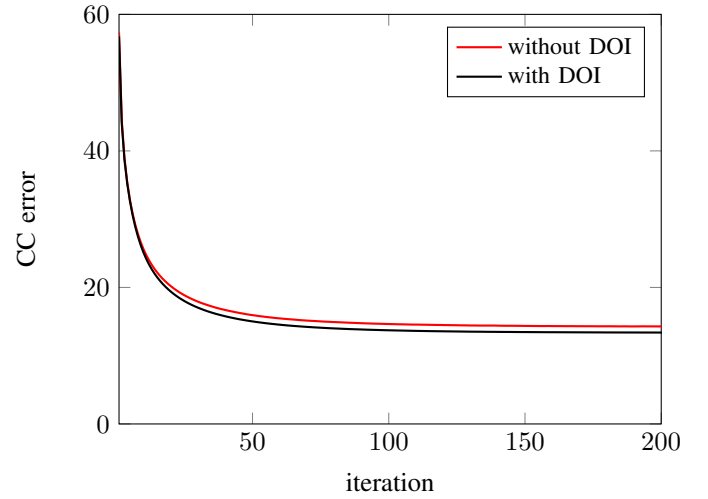


Fig. 5: CC error curves of the reconstructions, applying inflation in both forward and back projections.

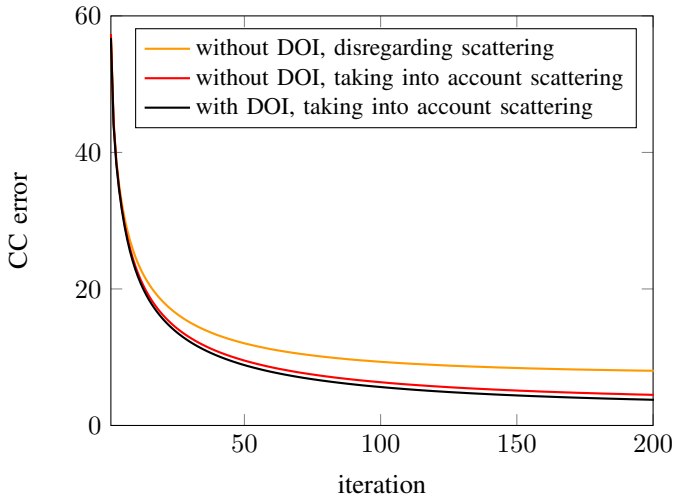


Fig. 4: CC error curves of the reconstructions, applying LOR filtering in forward and inflation in back projections.

Based on the obtained error curves, it can be concluded that ignoring scattering brings error into the reconstruction. If LOR filtering is applied in both forward and back projections (Figs. 3 and 6), it can be observed that at the beginning of the reconstruction, the models that disregard scattering perform better than the models that take into account scattering, which get better just later. The reason for this is that by ignoring scattering, the small-value elements of the system matrix are set to zero making the the matrix of forward and back projections better conditioned, and thereby improving the initial convergence speed, but changing the limiting value.

If we use inflation instead of LOR filtering in back projection (Figs. 4 and 7), the matrix conditioning is made better without sacrificing the limiting value. Thus, after 200 iterations the reconstruction reaches error 3.76 that is lower than the 5.28 CC error of LOR filtering applied also in back projection.

The worst result is obtained when we use inflation in both forward and back projection because inflation is just a rough

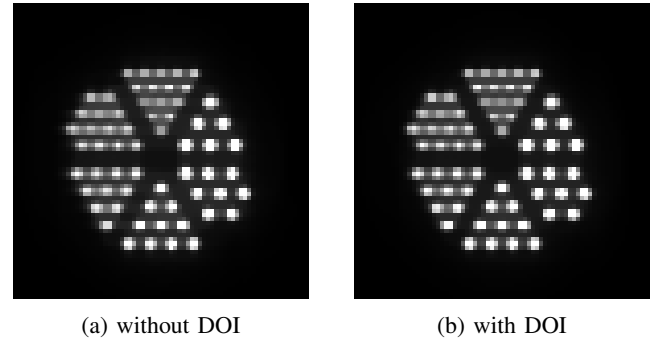


Fig. 6: Outputs of the reconstruction, applying LOR filtering in both forward and back projection.

estimate of the real detector model (Figs. 7 and 8).

VI. CONCLUSIONS

This paper proposed the application of 4D convolution as a means to simulate inter-crystal scattering in DOI-based PET reconstruction. The main contribution is that we could model Rayleigh and Compton scattering in the detector crystals in addition to absorption, making the simulation physically more

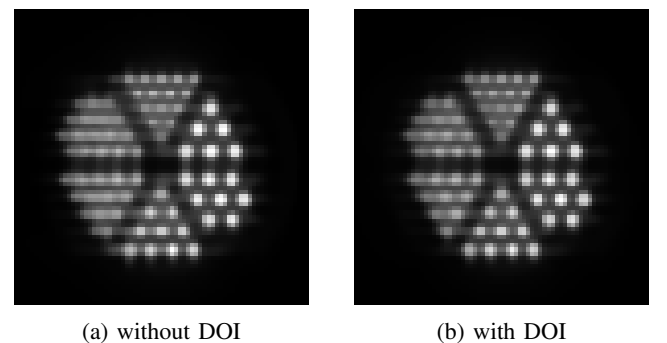
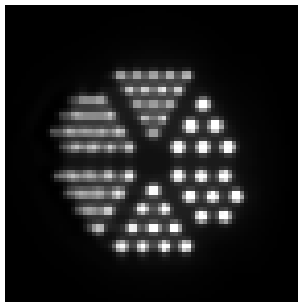
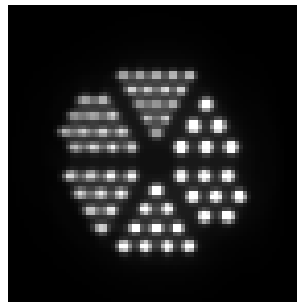


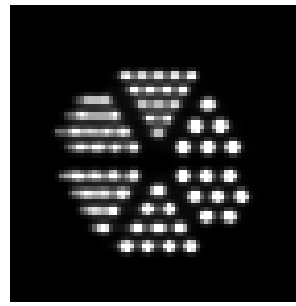
Fig. 8: Outputs of the reconstruction, applying inflation in both forward and back projection.



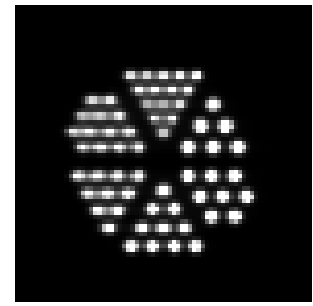
(a) without DOI, disregarding scattering



(b) with DOI, disregarding scattering



(c) without DOI, taking into account scattering



(d) with DOI, taking into account scattering

Fig. 7: Outputs of the reconstruction, applying LOR filtering in forward and inflation in back projection.

plausible. While the incorporation of a realistic detector model improves the quality of reconstructions, its computation time is negligible due to the efficient Monte Carlo evaluation scheme.

REFERENCES

- [1] A. J. Reader and H. Zaidi, "Advances in PET image reconstruction," *PET Clinics*, vol. 2, no. 2, pp. 173–190, 2007.
- [2] L. Szirmay-Kalos, A. Kacsó, M. Magdics, and B. Tóth, "Dynamic pet reconstruction on the gpu," *Periodica Polytechnica Electrical Engineering and Computer Science*, vol. 62, no. 4, pp. 134–143, 2018. [Online]. Available: <https://pp.bme.hu/eecs/article/view/11739>
- [3] H. T. van Dam, S. Seifert, R. Vinke, P. Dendooven, H. Löhner, F. J. Beekman, and D. R. Schaart, "A practical method for depth of interaction determination in monolithic scintillator PET detectors," *Physics in Medicine and Biology*, vol. 56, no. 13, pp. 4135–4145, 2011.
- [4] A. González-Montoro, A. Aguilar, G. Canizares, P. Conde, L. Hernández, L. F. Vidal, M. Galasso, A. Fabri, F. Sánchez, J. M. Benlloch, and A. J. González, "Performance study of a large monolithic lyso pet detector with accurate photon doi using retroreflector layers," *IEEE Transactions on Radiation and Plasma Medical Sciences*, vol. 1, no. 3, pp. 229–237, 2017.
- [5] F. Muller, D. Schug, P. Hallen, J. Grahe, and V. Schulz, "A novel doi positioning algorithm for monolithic scintillator crystals in pet based on gradient tree boosting," *IEEE Transactions on Radiation and Plasma Medical Sciences*, vol. 3, no. 4, p. 465474, 2019.
- [6] L. R. MacDonald and M. Dahlbom, "Parallax correction in pet using depth of interaction information," *IEEE Transactions on Nuclear Science*, vol. 45, no. 4, pp. 2232–2237, 1998.
- [7] M. Carles, C. Lerche, F. Snchez, F. Mora, and J. Benlloch, "Position correction with depth of interaction information for a small animal pet system," *Nuclear Instruments and Methods in Physics Research Section A: Accelerators, Spectrometers, Detectors and Associated Equipment*, vol. 648, pp. S176–S180, 2011.
- [8] J. G. Rogers, "A method for correcting the depth-of-interaction blurring in pet cameras," *IEEE Transactions on Medical Imaging*, vol. 14, no. 1, pp. 146–150, 1995.
- [9] R. S. Miyaoka, T. K. Lewellen, H. Yu, and D. L. McDaniel, "Design of a depth of interaction (doi) pet detector module," *IEEE Transactions on Nuclear Science*, vol. 45, no. 3, pp. 1069–1073, 1998.
- [10] M. Pizzichemi, G. Stringhini, T. Niknejad, Z. Liu, P. Lecoq, S. Tavernier, J. Varela, M. Paganoni, and E. Auffray, "A new method for depth of interaction determination in pet detectors," *Physics in Medicine and Biology*, vol. 61, pp. 4679–4698, 06 2016.
- [11] M. Ito, S. Hong, and J. Lee, "Positron emission tomography (pet) detectors with depth-of-interaction (doi) capability," *Biomedical Engineering Letters*, vol. 1, no. 2, pp. 70–81, 2011.
- [12] A. LaBella, P. Vaska, W. Zhao, and A. H. Goldan, "Convolutional neural network for crystal identification and gamma ray localization in pet," *IEEE Transactions on Radiation and Plasma Medical Sciences*, vol. 4, no. 4, pp. 461–469, 2020.
- [13] K. Kim, J. Dutta, A. Groll, G. E. Fakhri, L.-J. Meng, and Q. Li, "A novel depth-of-interaction rebinning strategy for ultrahigh resolution PET," *Physics in Medicine & Biology*, vol. 63, no. 16, p. 165011, 2018.
- [14] P. R. G. Virador, W. W. Moses, and R. H. Huesman, "Reconstruction in pet cameras with irregular sampling and depth of interaction capability," *IEEE Transactions on Nuclear Science*, vol. 45, no. 3, pp. 1225–1230, 1998.
- [15] T. Yamaya, N. Hagiwara, T. Obi, M. Yamaguchi, K. Kita, N. Ohya, K. Kitamura, T. Hasegawa, H. Haneishi, and H. Murayama, "Doi-pet image reconstruction with accurate system model reducing redundancy of imaging system," in *2002 IEEE Nuclear Science Symposium Conference Record*, vol. 2, 2002, pp. 1226–1230 vol.2.
- [16] D. Strul, R. B. Slates, M. Dahlbom, S. R. Cherry, and P. K. Marsden, "Use of an analytical model for optimizing the design of a small-animal pet scanner with doi capability," in *2000 IEEE Nuclear Science Symposium. Conference Record*, vol. 3, 2000, pp. 20/80–20/84 vol.3.
- [17] H. Takahashi, T. Yamaya, T. Kobayashi, K. Kitamura, T. Hasegawa, H. Murayama, and M. Suga, "System modeling of small bore doi-pet scanners for fast and accurate 3d image reconstruction," in *2007 IEEE Nuclear Science Symposium Conference Record*, vol. 5, 2007, pp. 3478–3481.
- [18] D. B. Keesing, D. Pal, J. A. O'Sullivan, S. Komarov, H. Wu, and Y. Tai, "System modeling of a doi-capable half-ring pet insert device for breast cancer imaging," in *2008 IEEE Nuclear Science Symposium Conference Record*, 2008, pp. 4218–4222.
- [19] J. Qi, R. M. Leahy, S. R. Cherry, A. Chatzioannou, and T. H. Farquhar, "High-resolution 3D Bayesian image reconstruction using the microPET small-animal scanner," *Physics in Medicine and Biology*, vol. 43, no. 4, p. 1001, 1998.
- [20] L. Szirmay-Kalos, M. Magdics, B. Tóth, and T. Bükki, "Averaging and Metropolis iterations for positron emission tomography," *IEEE Transactions on Medical Imaging*, vol. 32, no. 3, pp. 589–600, 2013.
- [21] L. Szirmay-Kalos, M. Magdics, and B. Tóth, "Multiple importance sampling for PET," *IEEE Transactions on Medical Imaging*, vol. 33, no. 4, pp. 970–978, 2014.
- [22] M. Magdics and L. Szirmay-Kalos, "Crystal Scattering Simulation for PET on the GPU," in *Eurographics 2011, Short paper*, 2011.
- [23] L. Szirmay-Kalos and L. Szécsi, "Deterministic importance sampling with error diffusion," *Computer Graphics Forum*, vol. 28, no. 4, pp. 1056–1064, 2009.
- [24] M. Magdics, L. Szirmay-Kalos, Á. Szlavecz, G. Hesz, B. Benyó, Á. Cserkaszkzy, J. Lantos, D. Légrády, Sz. Czifrus, A. Wirth, B. Kári, G. Patay, D. Völgyes, T. Bökki, P. Major, G. Németh, B. Domanos, "TeraTomo project: a fully 3D GPU based reconstruction code for exploiting the imaging capability of the NanoPET/CT system," in *World Molecular Imaging Congress*, 2010.
- [25] M. Magdics, L. Szirmay-Kalos, B. Tóth, D. Légrády, Á. Cserkaszkzy, L. Balkay, B. Domanos, D. Völgyes, G. Patay, P. Major, J. Lantos, and T. Bükki, "Performance Evaluation of Scatter Modeling of the GPU-based "Tera-Tomo" 3D PET Reconstruction," in *IEEE Nuclear Science Symposium and Medical Imaging*, 2011, pp. 4086–4088.